science.sciencemag.org/cgi/content/full/science.abb7498/DC1

Supplementary Materials for

Structure of the RNA-dependent RNA polymerase from COVID-19 virus

Yan Gao, Liming Yan, Yucen Huang, Fengjiang Liu, Yao Zhao, Lin Cao, Tao Wang, Qianqian Sun, Zhenhua Ming, Lianqi Zhang, Ji Ge, Litao Zheng, Ying Zhang, Haofeng Wang, Yan Zhu, Chen Zhu, Tianyu Hu, Tian Hua, Bing Zhang, Xiuna Yang, Jun Li, Haitao Yang, Zhijie Liu, Wenqing Xu, Luke W. Guddat, Quan Wang*, Zhiyong Lou*, Zihe Rao*

*Corresponding author. Email: wangq@shanghaitech.edu.cn (Q.W.); louzy@mail.tsinghua.edu.cn (Z.L.); raozh@mail.tsinghua.edu.cn (Z.R.)

Published 10 April 2020 on *Science* First Release
DOI: 10.1126/science.abb7498

This PDF file includes:

Materials and Methods
Figs. S1 to S7
Table S1
Caption for Movie S1
References

Other Supplementary Material for this manuscript includes the following:
(available at science.sciencemag.org/cgi/content/full/science.abb7498/DC1)

Movie S1 (.mp4)

Materials and Methods

Protein production and purification

The COVID-19 virus nsp12 (GenBank: MN908947) gene was cloned into a modified pET-22a vector, with the C-terminus possessing a 10 × His-tag. The plasmids were transformed into *E. coli* BL21 (DE3), and the transformed cells were cultured at 37 °C in LB media containing 100 mg/L ampicillin. After the OD_{600} reached 0.8, the culture was cooled to 16 °C and supplemented with 0.5 mM IPTG. After overnight induction, the cells were harvested through centrifugation, and the pellets were resuspended in lysis buffer (20 mM Tris-HCl, pH 8.0, 150 mM NaCl, 4 mM $MgCl_2$, 10% glycerol) and homogenized with an ultra-high-pressure cell disrupter at 4 °C. The insoluble material was removed through centrifugation at 12,000 rpm. The fusion protein was first purified by Ni-NTA affinity chromatography and then further purified by passage through a Hitrap Q ion-exchange column (GE Healthcare, USA) before loading onto a Superdex 200 10/300 Increase column (GE Healthcare, USA) in a buffer containing 20 mM Tris-HCl, pH 7.5, 250 mM NaCl and 4 mM $MgCl_2$. Purified nsp12 was concentrated to 4 mg/mL and stored at 4 °C.
Full-length COVID-19 virus nsp7 and nsp8 were co-expressed in *E. coli* BL21 (DE3) cells as a no-tagged protein and a 6 × His-SUMO fusion protein, respectively. After purification by Ni-NTA (Novagen) affinity chromatography, the nsp7-nsp8 complex was eluted through on-column tag cleavage by ULP protease. The eluate was further purified by Hitrap Q ion-exchange column (GE Healthcare, USA) and a Superdex 200 10/300 Increase column (GE Healthcare, USA) in a buffer containing 20 mM Tris-HCl, pH 7.5, 250 mM NaCl and 4 mM $MgCl_2$.
For assembling stable nsp12-nsp7-nsp8 complex, purified nsp12 was incubated with nsp7 and nsp8 at 4 ℃ for three hours, at a molar ratio of 1: 2: 2 in a buffer containing 20 mM Tris-HCl, pH 7.5, 250 mM NaCl and 4 mM $MgCl_2$. For the sample in reduced condition, the complex was further transferred to a reducing buffer containing 20 mM Tris-HCl, pH 7.0, 250 mM NaCl and 4 mM $MgCl_2$, 4 mM DTT using a centrifugal ultrafiltration device (Amicon® Ultra Filters).

Cryo-EM sample preparation and data collection

In total, 3 μL of protein solution at 0.7 mg/mL (added with 0.025% DDM, both samples the same) was applied onto a H_2/O_2 glow-discharged, 300-mesh Quantifoil R1.2/1.3 grid (Quantifoil, Micro Tools GmbH, Germany). The grid was then blotted for 3.0 s with a blot force of 0 at 8°C and 100% humidity and plunge-frozen in liquid ethane using a Vitrobot (Thermo Fisher Scientific, USA). Cryo-EM data were collected with a 300 keV Titan Krios electron microscope (Thermo Fisher Scientific, USA) and a K2 Summit direct electron detector (Gatan, USA). Images were recorded at EFTEM with a 165000× magnification and calibrated super-resolution pixel size 0.82 Å/pixel. The exposure time was set to 5 s with a total accumulated dose of 60 electrons per $Å^2$. All images were automatically recorded using SerialEM (*18*). For Dataset-1, a total of 7,994 images were collected with a defocus range from 1.0 μm to 1.8 μm. For Dataset-2 (under reducing conditions), a total of 8494 images were collected with a defocus range from 1.1 μm to 2.0 μm. Statistics for data collection and refinement are in Table S1.

Cryo-EM image processing

All dose-fractioned images were motion-corrected and dose-weighted by MotionCorr2 software (*19*) and their contrast transfer functions were estimated by cryoSPARC patch CTF estimation. For Dataset-1, a total of 2,334,248 particles were auto-picked using blob picker and extracted with a box size of 300 pixels in cryoSPARC (*20*). The following 2D, 3D classifications

and refinements were all performed in cryoSPARC. 918,133 particles were selected after two rounds of 2D classification. 100,000 particles were used to do Ab-Initio reconstruction in five classes, and then these five classes were used as 3D volume templates for heterogeneous refinement with all selected particles, with 110,176 particles converged into one class. Next, this particle set was used to perform homogeneous refinement, yielding a resolution of 3.1 Å. After local refinement, the final resolution reached 2.9 Å. For Dataset-2, the image processing was conducted using a similar pipeline. 753,481 particles were auto-picked initially, and 145,388 particles were selected after final heterogeneous refinement. The resolution reached 2.99 Å after non-uniform refinement and 2.95 Å after local refinement with a mask.

Model building and refinement

To solve the structure of the COVID-19 virus nsp12-nsp7-nsp8 complex, the structure of the SARS-CoV nsp12 (*9*) and nsp7-8 (*21*) were individually placed and rigid-body fitted into the cryo-EM map using UCSF Chimera (*22*). After the corresponding amino acids were replaced with those from COVID-19 virus, the model was manually built in Coot 0.8 (*23*) with the guidance of the cryo-EM map, and in combination with real space refinement using Phenix 1.9 (*24*). The data validation statistics are shown in Table S1.

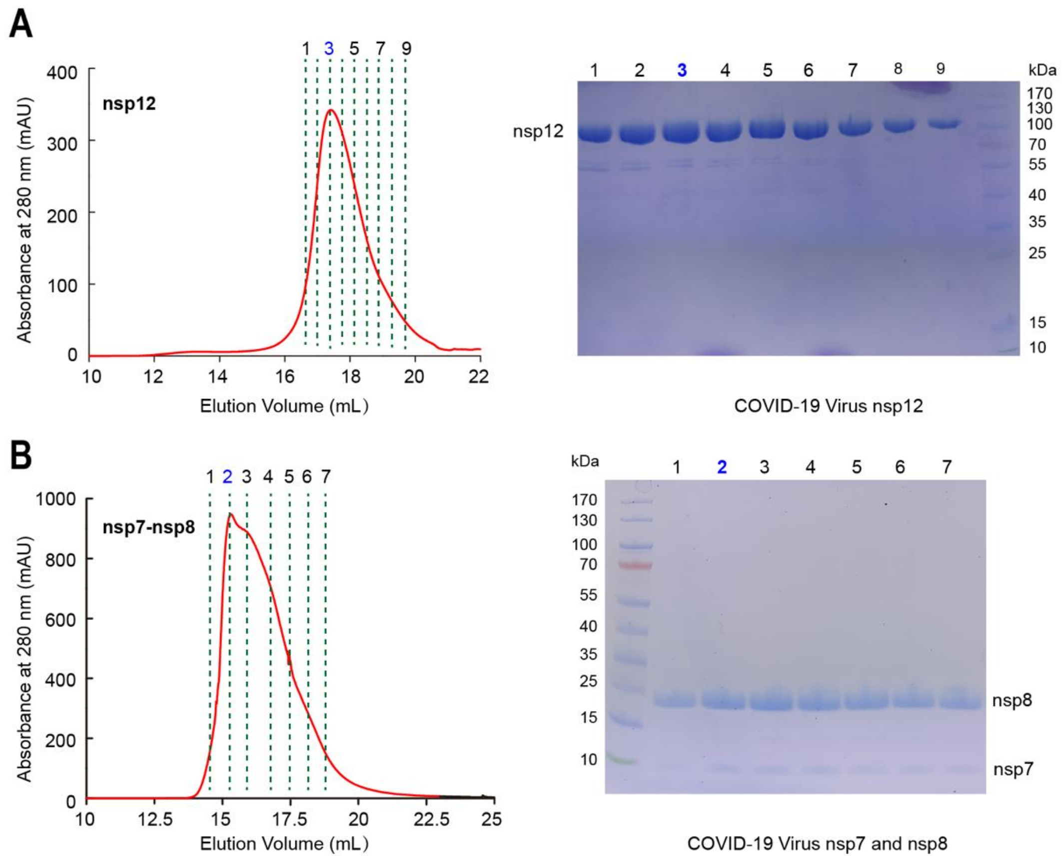

Fig. S1.

The purification of COVID-19 virus nsp12 and nsp12-nsp7-nsp8 complex using a Superdex 200 10/30 column. **(A)** Size-exclusion chromatogram of the affinity-purified the COVID-19 virus nsp12 and **(B)** nsp7-nsp8 complex. Fractions from the gel filtration peaks were pooled. The target proteins were analyzed by SDS-PAGE. Standard protein markers are shown in the first lane.

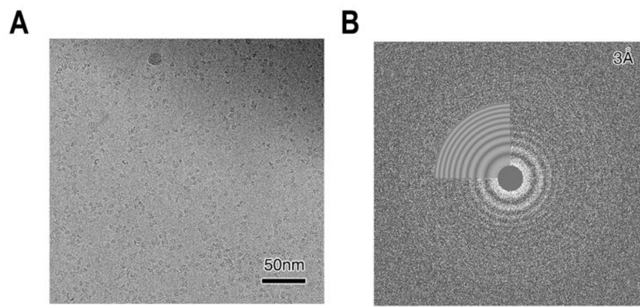
A
B
50nm
3Å

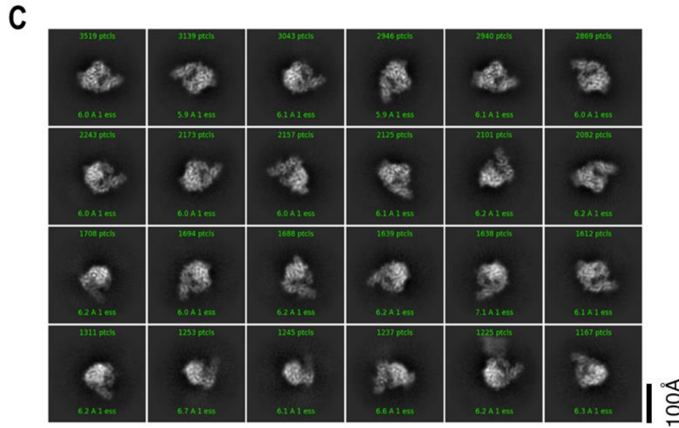
C
100Å

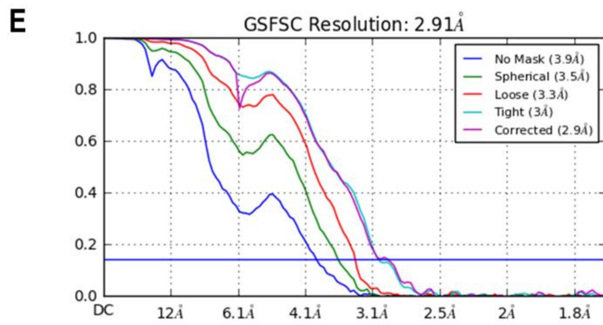
E
GSFSC Resolution: 2.91Å
No Mask (3.9Å)
Spherical (3.5Å)
Loose (3.3Å)
Tight (3Å)
Corrected (2.9Å)
DC
12Å
6.1Å
4.1Å
3.1Å
2.5Å
2Å
1.8Å

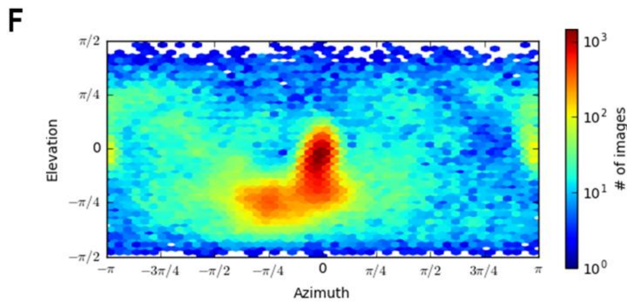
F
Elevation
Azimuth
# of images

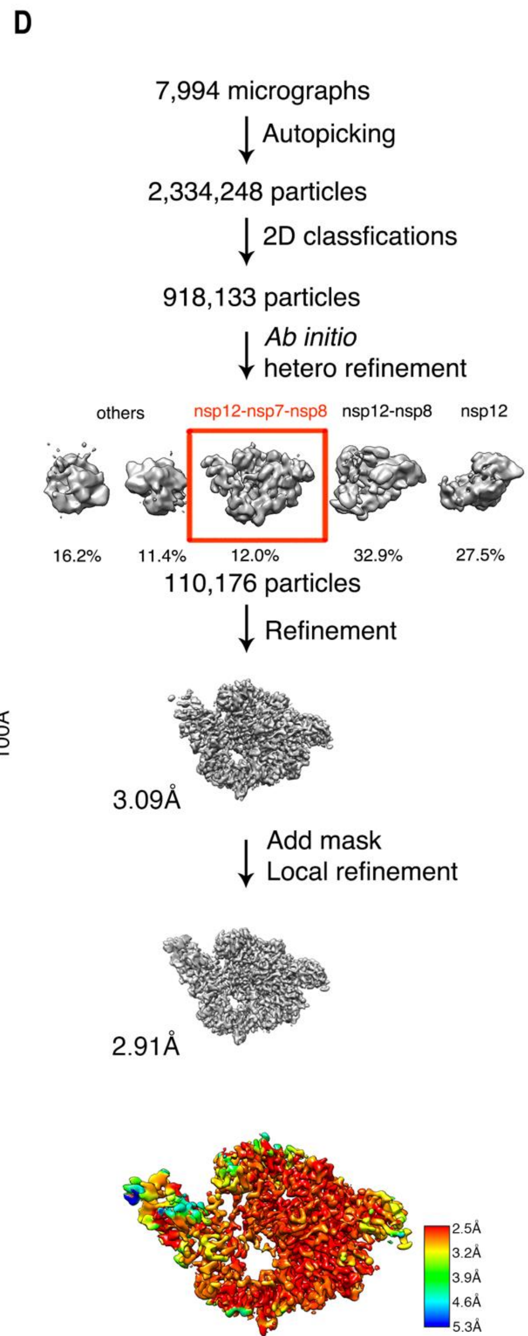
D
7,994 micrographs
Autopicking
2,334,248 particles
2D classfications
918,133 particles
Ab initio
hetero refinement
others
nsp12-nsp7-nsp8
nsp12-nsp8
nsp12
16.2%
11.4%
12.0%
32.9%
27.5%
110,176 particles
Refinement
3.09Å
Add mask
Local refinement
2.91Å
2.5Å
3.2Å
3.9Å
4.6Å
5.3Å

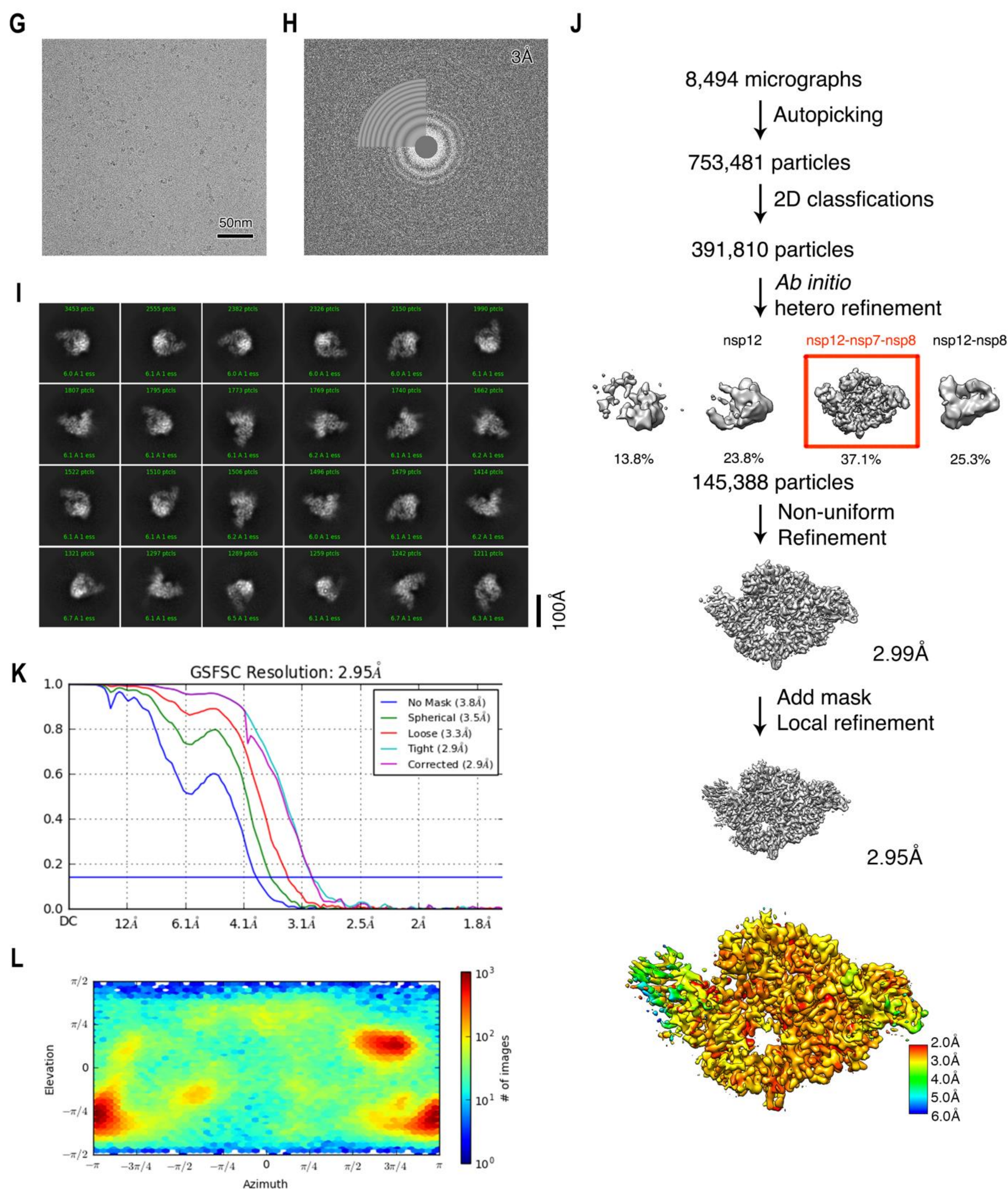

Fig. S2.

Cryo-EM reconstruction. (A) Raw image of the nsp12-nsp7-nsp8 complex particles in vitreous ice recorded at defocus values of -1.0 to -1.8 µm. Scale bar, 50 nm. **(B)** Power spectrum of the image shown in (A), with an indication of the spatial frequency corresponding to 3.0 Å resolution. **(C)** Representative class averages. The edge of each square is 246 Å. **(D)** The data processing

scheme. Overview of nsp12-nsp7-nsp8 reconstruction is shown in the bottom panel along with Local resolution. **(E)** Fourier shell correlation (FSC) of the final 3D reconstruction following gold standard refinement. FSC curves are plotted before and after masking. **(F)** Angular distribution heatmap of particles used for the refinement. **(G-I)** Data processing procedure and corresponding results for Dataset-2 (collected under reducing conditions).

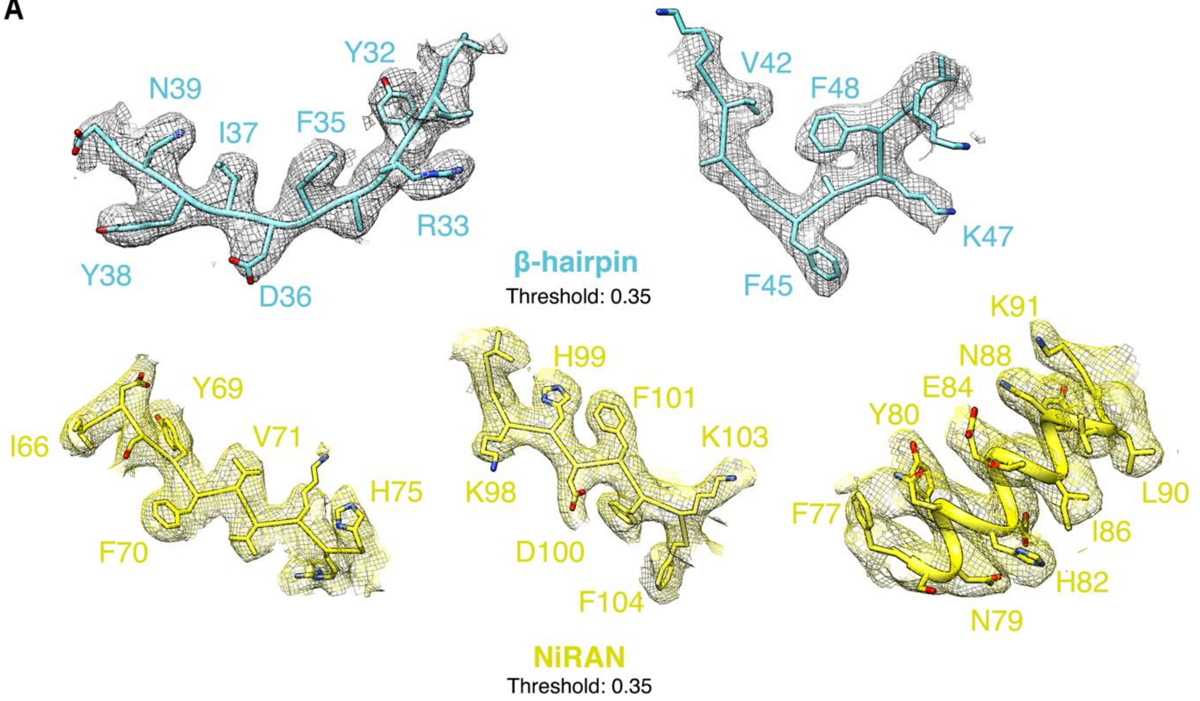
A
Y32
N39
I37
F35
R33
Y38
D36
V42
F48
K47
F45
β-hairpin
Threshold: 0.35
Y69
I66
V71
H75
F70
H99
F101
K103
K98
D100
F104
K91
N88
E84
Y80
F77
L90
I86
H82
N79
NiRAN
Threshold: 0.35

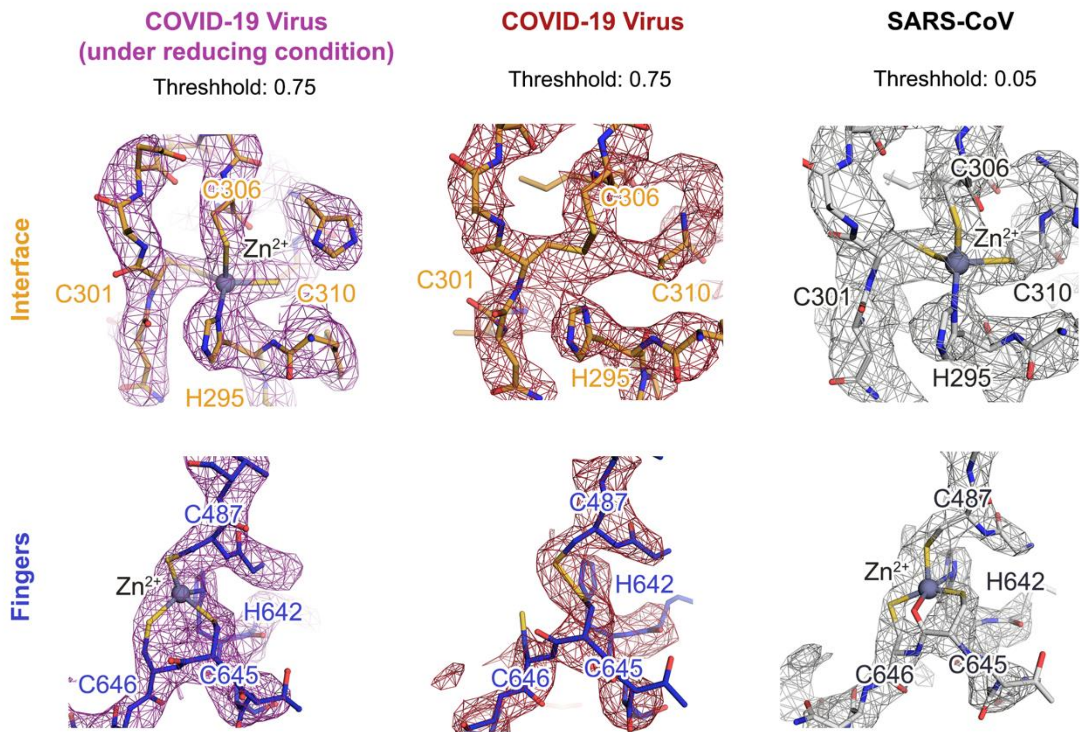
B
COVID-19 Virus
(under reducing condition)
Threshhold: 0.75
COVID-19 Virus
Threshhold: 0.75
SARS-CoV
Threshhold: 0.05
Interface
C306
Zn2+
C301
C310
H295
Fingers
C487
H642
C646
C645

Fig. S3.

Cryo-EM map of β-hairpin (A) and disulfide bonds (B). (A) Structure and representative map of β-hairpin and NiRAN. **(B)** Raw cryo-EM map (mesh) for the nsp12-nsp7-nsp8 complex is shown in magenta and red (COVID-19 virus) for Dataset-2 and Dataset-1, respectively or grey (SARS-CoV, EMD-0520). Structures near the disulfide bond region of the Interface domain (orange) and Fingers domain (deep blue) are shown as stick models. The corresponding region in SARS-CoV (PDB ID: 6NUR) is shown on the right.

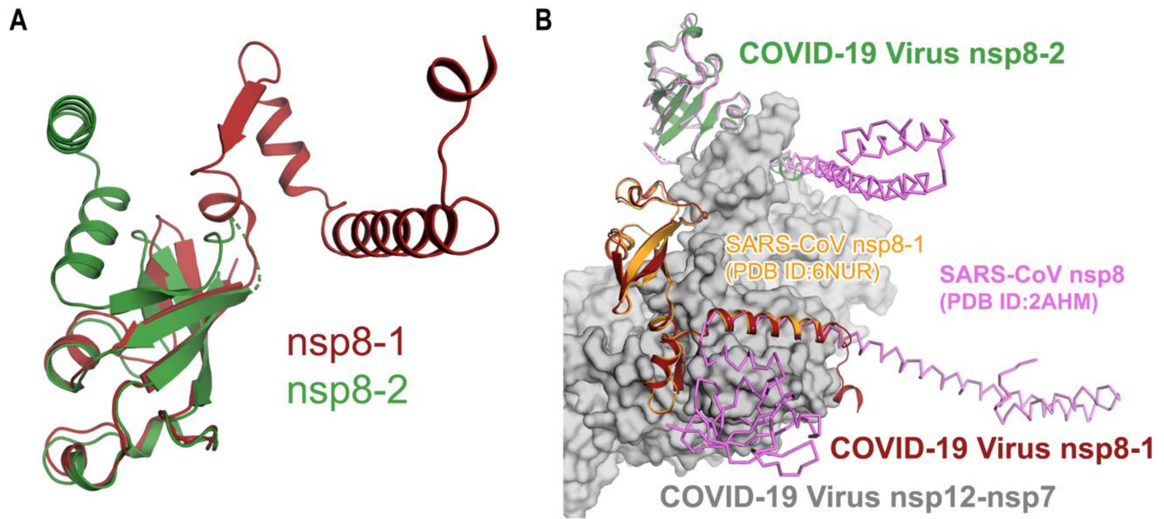
A
nsp8-1
nsp8-2
B
COVID-19 Virus nsp8-2
SARS-CoV nsp8-1
(PDB ID:6NUR)
SARS-CoV nsp8
(PDB ID:2AHM)
COVID-19 Virus nsp8-1
COVID-19 Virus nsp12-nsp7

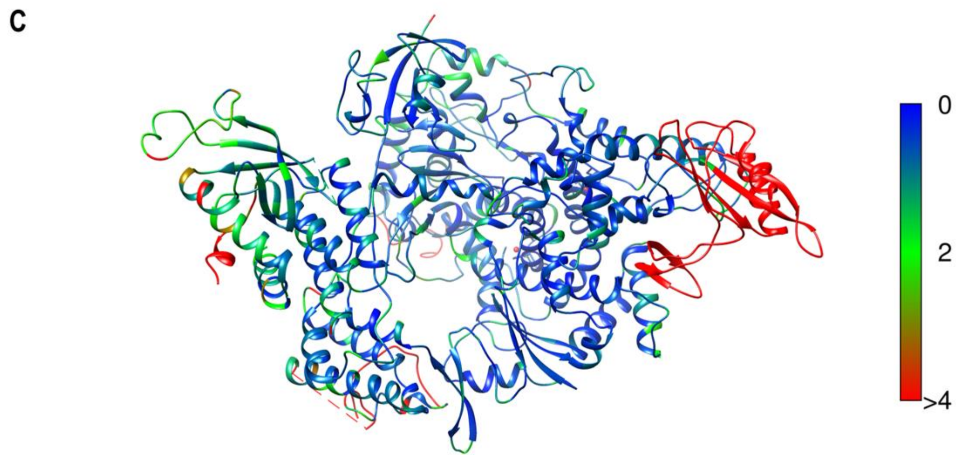
C
0
2
>4

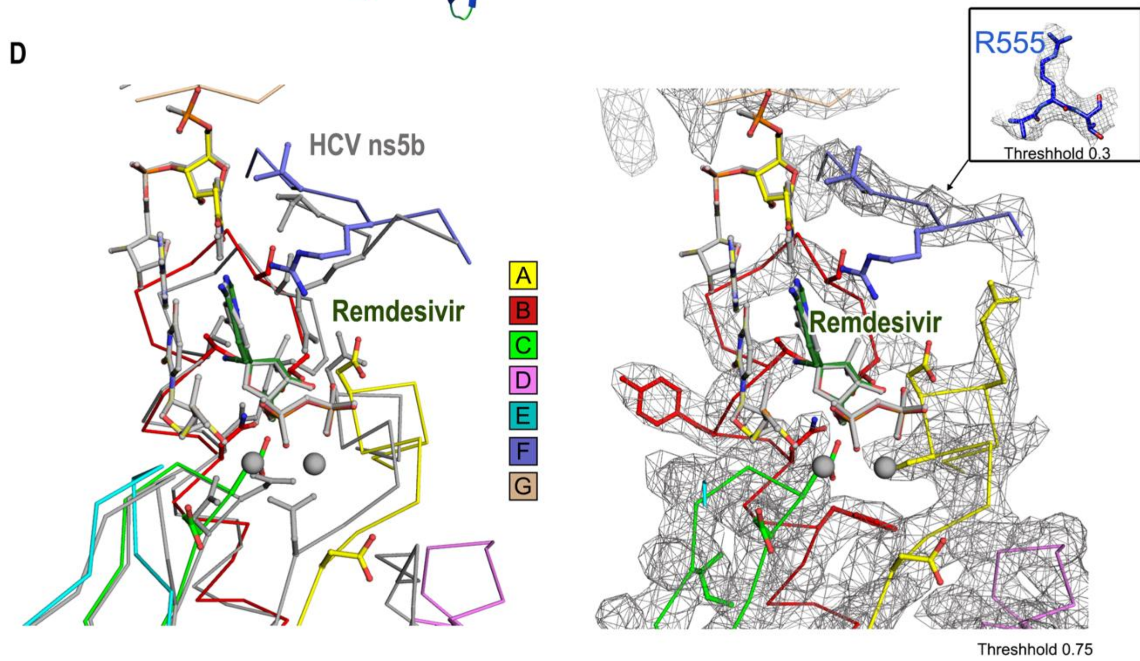
D
HCV ns5b
Remdesivir
A
B
C
D
E
F
G
R555
Threshhold 0.3
Remdesivir
Threshhold 0.75

Fig. S4.

Structure comparisons. (A) Comparison of two nsp8 molecules bound to COVID-19 virus nsp12. The nsp8-1 (in red) refers to the individual nsp8 molecule bound to nsp12. The nsp8-2 (in green) refers to the nsp8 molecule in nsp7-nsp8 pair. **(B)** An overview of the complex showing how two nsp8 units bind with different conformations to nsp12. **(C)** The structure difference between COVID-19 virus nsp12-nsp7-nsp8 complex and SARS-CoV nsp12-nsp7-nsp8 complex (color by RMSD-Full in Chimera). **(D)** Comparison of COVID-19 virus nsp12 (in color) and HCV ns5b (in grey). The experimental EM map covering the active site of COVID-19 virus nsp12 is shown as mesh in the right panel.

COVID-19 Virus nsp12-nsp7-nsp8 complex (Dataset-1)		
β-hairpin	Contact*	Target Residues
R33	1,1	D126,K121
A34	1,1	D126,A125
D36	1,5,2	D208,Y728,S236
Y38	2,1,2	Y728,H725,E729
N39	4	H725
A43	3	Q724
G44	1	Y728
F45	1	S709
A46	2	S709
K47	2	Y129
F48	2	D711

COVID-19 Virus nsp12-nsp7-nsp8 complex under reducing condition (Dataset-2)		
β-hairpin	Contact*	Target Residues
R33	1	Y122
A34	1	D126
F35	1	D208
D36	1,1,1	D208,Y728,L240
Y38	1,1,1,3	Y728,H725,R733,E729
N39	2	H725
A43	3	Q724
F45	1	L708
A46	1	S709
F48	1	D711

Fig. S5.

Interaction between the β-hairpin and other domains. *Numbers represent the number of atom-to-atom contacts between the residues of β-hairpin and the residues in other domains. These were calculated by the Contact program in the CCP4 suite (with a distance cutoff of 3.5 Å).

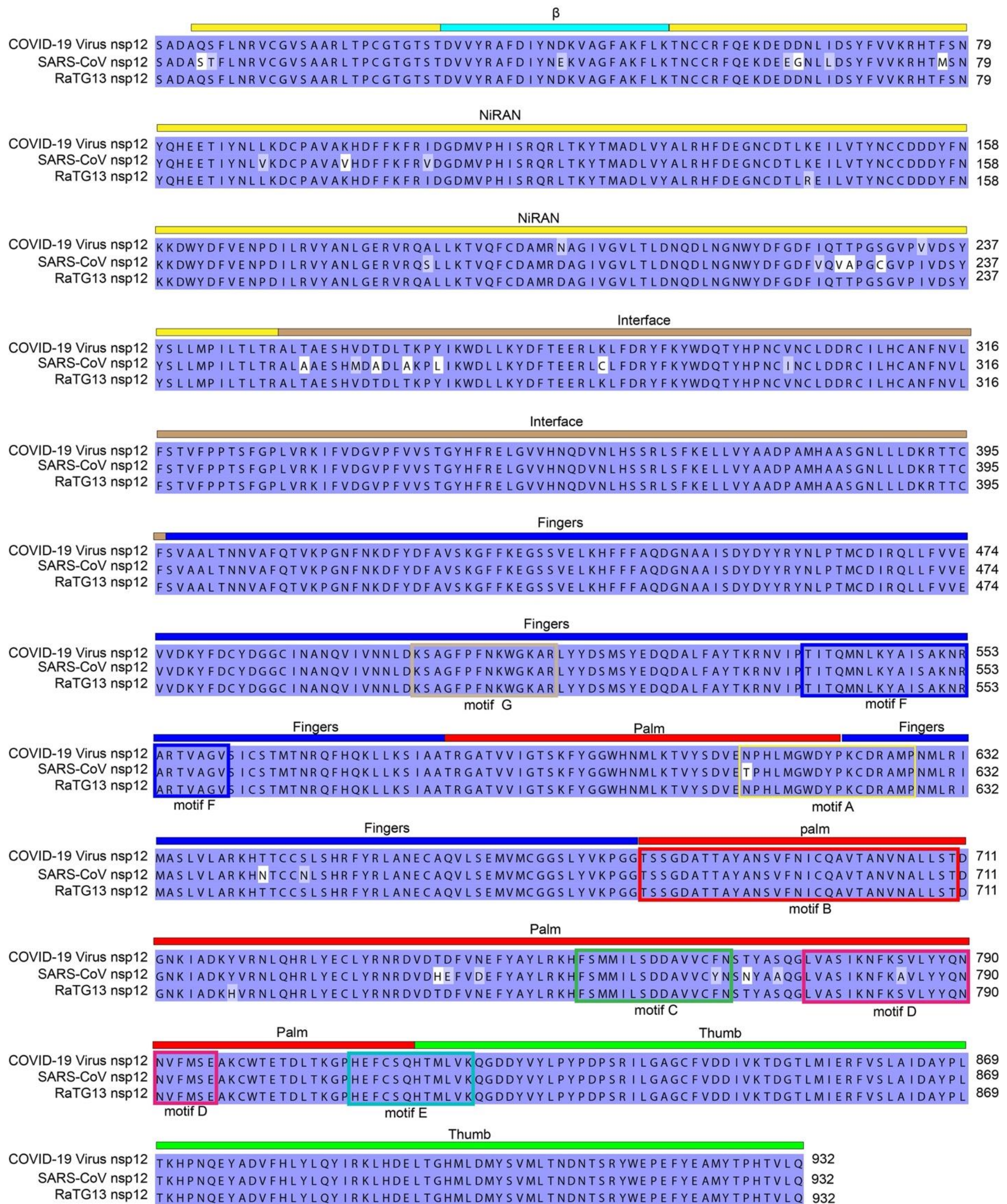

Fig. S6.

Sequence alignment of nsp12 proteins encoded by COVID-19 virus, SARS-CoV and RaTG13. The residues with blue, light blue or white backgrounds indicate the identical, conserved

or non-conserved residues, respectively. Domain arrangement and key RdRp motifs are highlighted using the same color scheme as in Fig. 1.

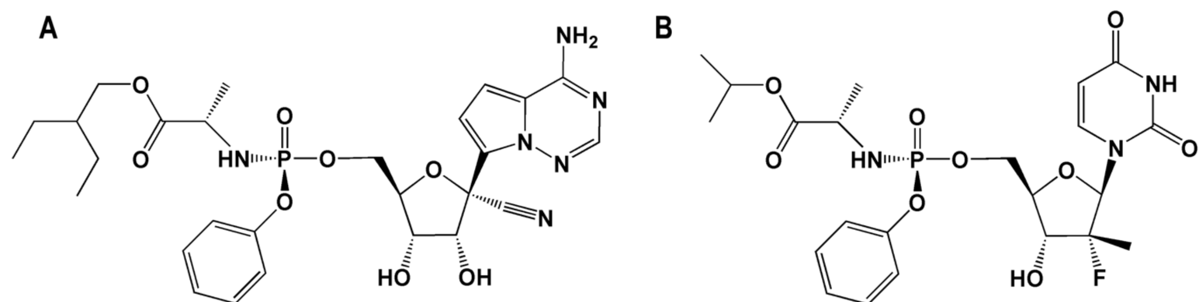

Fig. S7.
Chemical structures of the prodrugs of (A) remdesivir and (B) sofosbuvir.

	COVID-19 Virus nsp12-nsp7-nsp8 complex	COVID-19 Virus nsp12-nsp7-nsp8 complex under reducing condition
PDB entry	6M71	7BTF
EMDB entry	30127	30178
Data collection and processing		
Magnification	165,000	165,000
Voltage (keV)	300	300
Electron exposure (e^-/Å^2)	60.00	60.00
Defocus range (μm)	-1.8 to -1.0	-2.0 to -1.1
Pixel size (Å)	0.82	0.82
Symmetry imposed	C1	C1
Initial particle images (no.)	2,334,248	753,481
Final particle images (no.)	110,176	145,388
Map global resolution (Å)	2.91	2.95
Global resolution FSC threshold	0.143	0.143
Map local resolution range (Å)	1.8-7.8	1.8-7.5
Local resolution FSC threshold	0.143	0.143
Refinement		
Model resolution (Å)	2.9	2.9
FSC threshold	0.143	0.143
Model resolution range (Å)	□ to 2.9	□ to 2.9
Map sharpening *B* factor (Å^2)	80.2	97.6
Model composition		
Non-hydrogen atoms	8,550	9,783
Protein residues	1,077	1,227
Ligands	0	2
B factors (Å^2)		
Protein	67.69	58.46
Ligand		62.28
R.m.s. deviations		
Bond lengths (Å)	0.003	0.004
Bond angles (°)	0.551	0.552
Validation		
MolProbity score	1.71	1.58
Clashscore	8.58	4.91
Poor rotamers (%)	0.11	0.00
Ramachandran plot		
Favored (%)	96.31	95.31
Allowed (%)	3.69	4.69
Disallowed (%)	0.00	0.00
Model coverage		
Chain A	V31-K50; Y69-R74; T76-F102; P112-V335; G337-L895; M906-E919	A4-T896; M902-Q932
Chain B	E77-A191	M67-N192
Chain C	K2-L71	S1-E73
Chain D	T84-I132	T84-L122; K127-A191

Table S1.
Cryo-EM data statistics.

Movie S1.
Experimental cryo-EM map of nsp12 N-terminal region (A4 to R118)

References and Notes

1. J. F. Chan, S. Yuan, K.-H. Kok, K. K.-W. To, H. Chu, J. Yang, F. Xing, J. Liu, C. C.-Y. Yip, R. W.-S. Poon, H.-W. Tsoi, S. K.-F. Lo, K.-H. Chan, V. K.-M. Poon, W.-M. Chan, J. D. Ip, J.-P. Cai, V. C.-C. Cheng, H. Chen, C. K.-M. Hui, K.-Y. Yuen, A familial cluster of pneumonia associated with the 2019 novel coronavirus indicating person-to-person transmission: A study of a family cluster. *Lancet* **395**, 514–523 (2020). doi:10.1016/S0140-6736(20)30154-9 Medline

2. N. Chen, M. Zhou, X. Dong, J. Qu, F. Gong, Y. Han, Y. Qiu, J. Wang, Y. Liu, Y. Wei, J. Xia, T. Yu, X. Zhang, L. Zhang, Epidemiological and clinical characteristics of 99 cases of 2019 novel coronavirus pneumonia in Wuhan, China: A descriptive study. *Lancet* **395**, 507–513 (2020). doi:10.1016/S0140-6736(20)30211-7 Medline

3. F. Wu, S. Zhao, B. Yu, Y.-M. Chen, W. Wang, Z.-G. Song, Y. Hu, Z.-W. Tao, J.-H. Tian, Y.-Y. Pei, M.-L. Yuan, Y.-L. Zhang, F.-H. Dai, Y. Liu, Q.-M. Wang, J.-J. Zheng, L. Xu, E. C. Holmes, Y.-Z. Zhang, A new coronavirus associated with human respiratory disease in China. *Nature* **579**, 265–269 (2020). doi:10.1038/s41586-020-2008-3 Medline

4. P. Zhou, X.-L. Yang, X.-G. Wang, B. Hu, L. Zhang, W. Zhang, H.-R. Si, Y. Zhu, B. Li, C.-L. Huang, H.-D. Chen, J. Chen, Y. Luo, H. Guo, R.-D. Jiang, M.-Q. Liu, Y. Chen, X.-R. Shen, X. Wang, X.-S. Zheng, K. Zhao, Q.-J. Chen, F. Deng, L.-L. Liu, B. Yan, F.-X. Zhan, Y.-Y. Wang, G.-F. Xiao, Z.-L. Shi, A pneumonia outbreak associated with a new coronavirus of probable bat origin. *Nature* **579**, 270–273 (2020). doi:10.1038/s41586-020-2012-7 Medline

5. J. Ziebuhr, The coronavirus replicase. *Curr. Top. Microbiol. Immunol.* **287**, 57–94 (2005). doi:10.1007/3-540-26765-4_3 Medline

6. L. Subissi, C. C. Posthuma, A. Collet, J. C. Zevenhoven-Dobbe, A. E. Gorbalenya, E. Decroly, E. J. Snijder, B. Canard, I. Imbert, One severe acute respiratory syndrome coronavirus protein complex integrates processive RNA polymerase and exonuclease activities. *Proc. Natl. Acad. Sci. U.S.A.* **111**, E3900–E3909 (2014). doi:10.1073/pnas.1323705111 Medline

7. M. Wang, R. Cao, L. Zhang, X. Yang, J. Liu, M. Xu, Z. Shi, Z. Hu, W. Zhong, G. Xiao, Remdesivir and chloroquine effectively inhibit the recently emerged novel coronavirus (2019-nCoV) in vitro. *Cell Res.* **30**, 269–271 (2020). doi:10.1038/s41422-020-0282-0 Medline

8. M. L. Holshue, C. DeBolt, S. Lindquist, K. H. Lofy, J. Wiesman, H. Bruce, C. Spitters, K. Ericson, S. Wilkerson, A. Tural, G. Diaz, A. Cohn, L. Fox, A. Patel, S. I. Gerber, L. Kim, S. Tong, X. Lu, S. Lindstrom, M. A. Pallansch, W. C. Weldon, H. M. Biggs, T. M. Uyeki, S. K. Pillai, Washington State 2019-nCoV Case Investigation Team, First Case of 2019 Novel Coronavirus in the United States. *N. Engl. J. Med.* **382**, 929–936 (2020). doi:10.1056/NEJMoa2001191 Medline

9. R. N. Kirchdoerfer, A. B. Ward, Structure of the SARS-CoV nsp12 polymerase bound to nsp7 and nsp8 co-factors. *Nat. Commun.* **10**, 2342 (2019). doi:10.1038/s41467-019-10280-3 Medline

10. K. C. Lehmann, A. Gulyaeva, J. C. Zevenhoven-Dobbe, G. M. C. Janssen, M. Ruben, H. S. Overkleeft, P. A. van Veelen, D. V. Samborskiy, A. A. Kravchenko, A. M. Leontovich, I. A. Sidorov, E. J. Snijder, C. C. Posthuma, A. E. Gorbalenya, Discovery of an essential nucleotidylating activity associated with a newly delineated conserved domain in the RNA polymerase-containing protein of all nidoviruses. *Nucleic Acids Res.* **43**, 8416–8434 (2015). doi:10.1093/nar/gkv838 Medline

11. Y. Zhai, F. Sun, X. Li, H. Pang, X. Xu, M. Bartlam, Z. Rao, Insights into SARS-CoV transcription and replication from the structure of the nsp7-nsp8 hexadecamer. *Nat. Struct. Mol. Biol.* **12**, 980–986 (2005). doi:10.1038/nsmb999 Medline

12. S. M. McDonald, RNA synthetic mechanisms employed by diverse families of RNA viruses. *Wiley Interdiscip. Rev. RNA* **4**, 351–367 (2013). doi:10.1002/wrna.1164 Medline

13. T. C. Appleby, J. K. Perry, E. Murakami, O. Barauskas, J. Feng, A. Cho, D. Fox 3rd, D. R. Wetmore, M. E. McGrath, A. S. Ray, M. J. Sofia, S. Swaminathan, T. E. Edwards, Structural basis for RNA replication by the hepatitis C virus polymerase. *Science* **347**, 771–775 (2015). doi:10.1126/science.1259210 Medline

14. P. Gong, O. B. Peersen, Structural basis for active site closure by the poliovirus RNA-dependent RNA polymerase. *Proc. Natl. Acad. Sci. U.S.A.* **107**, 22505–22510 (2010). doi:10.1073/pnas.1007626107 Medline

15. T. K. Warren, R. Jordan, M. K. Lo, A. S. Ray, R. L. Mackman, V. Soloveva, D. Siegel, M. Perron, R. Bannister, H. C. Hui, N. Larson, R. Strickley, J. Wells, K. S. Stuthman, S. A. Van Tongeren, N. L. Garza, G. Donnelly, A. C. Shurtleff, C. J. Retterer, D. Gharaibeh, R. Zamani, T. Kenny, B. P. Eaton, E. Grimes, L. S. Welch, L. Gomba, C. L. Wilhelmsen, D. K. Nichols, J. E. Nuss, E. R. Nagle, J. R. Kugelman, G. Palacios, E. Doerffler, S. Neville, E. Carra, M. O. Clarke, L. Zhang, W. Lew, B. Ross, Q. Wang, K. Chun, L. Wolfe, D. Babusis, Y. Park, K. M. Stray, I. Trancheva, J. Y. Feng, O. Barauskas, Y. Xu, P. Wong, M. R. Braun, M. Flint, L. K. McMullan, S.-S. Chen, R. Fearns, S. Swaminathan, D. L. Mayers, C. F. Spiropoulou, W. A. Lee, S. T. Nichol, T. Cihlar, S. Bavari, Therapeutic efficacy of the small molecule GS-5734 against Ebola virus in rhesus monkeys. *Nature* **531**, 381–385 (2016). doi:10.1038/nature17180 Medline

16. E. J. Gane, C. A. Stedman, R. H. Hyland, X. Ding, E. Svarovskaia, W. T. Symonds, R. G. Hindes, M. M. Berrey, Nucleotide polymerase inhibitor sofosbuvir plus ribavirin for hepatitis C. *N. Engl. J. Med.* **368**, 34–44 (2013). doi:10.1056/NEJMoa1208953 Medline

17. C. Chen, J. Huang, Z. Cheng, J. Wu, S. Chen, Y. Zhang, B. Chen, M. Lu, Y. Luo, J. Zhang, P. Yin, X. Wang, Favipiravir versus Arbidol for COVID-19: A Randomized Clinical Trial. medRxiv 2020.03.17.20037432 [Preprint]. 27 March 2020. https://doi.org/10.1101/2020.03.17.20037432.

18. D. N. Mastronarde, Automated electron microscope tomography using robust prediction of specimen movements. *J. Struct. Biol.* **152**, 36–51 (2005). doi:10.1016/j.jsb.2005.07.007 Medline

19. S. Q. Zheng, E. Palovcak, J.-P. Armache, K. A. Verba, Y. Cheng, D. A. Agard, MotionCor2: Anisotropic correction of beam-induced motion for improved cryo-electron microscopy. *Nat. Methods* **14**, 331–332 (2017). doi:10.1038/nmeth.4193 Medline

20. A. Punjani, J. L. Rubinstein, D. J. Fleet, M. A. Brubaker, cryoSPARC: Algorithms for rapid unsupervised cryo-EM structure determination. *Nat. Methods* **14**, 290–296 (2017). doi:10.1038/nmeth.4169 Medline

21. S. Li, Q. Zhao, Y. Zhang, Y. Zhang, M. Bartlam, X. Li, Z. Rao, New nsp8 isoform suggests mechanism for tuning viral RNA synthesis. *Protein Cell* **1**, 198–204 (2010). doi:10.1007/s13238-010-0028-8 Medline

22. E. F. Pettersen, T. D. Goddard, C. C. Huang, G. S. Couch, D. M. Greenblatt, E. C. Meng, T. E. Ferrin, UCSF Chimera—A visualization system for exploratory research and analysis. *J. Comput. Chem.* **25**, 1605–1612 (2004). doi:10.1002/jcc.20084 Medline

23. P. Emsley, B. Lohkamp, W. G. Scott, K. Cowtan, Features and development of Coot. *Acta Cryst.* **D66**, 486–501 (2010). doi:10.1107/S0907444910007493 Medline

24. P. V. Afonine, R. W. Grosse-Kunstleve, N. Echols, J. J. Headd, N. W. Moriarty, M. Mustyakimov, T. C. Terwilliger, A. Urzhumtsev, P. H. Zwart, P. D. Adams, Towards automated crystallographic structure refinement with phenix.refine. *Acta Cryst.* **D68**, 352–367 (2012). doi:10.1107/S0907444912001308 Medline